

Nonreflecting outlet boundary conditions for incompressible flows using SPH

Carlos E. Alvarado-Rodríguez^a, Jaime Klapp^{b,c,*}, Leonardo Di G. Sigalotti^d, José M. Domínguez^e, Eduardo de la Cruz Sánchez^b

^a*Departamento de Ingeniería Química, DCNyE, Universidad de Guanajuato, Noria Alta S/N, 36000 Guanajuato, Guanajuato, Mexico*

^b*Departamento de Física, Instituto Nacional de Investigaciones Nucleares (ININ), Carretera México-Toluca S/N, La Marquesa, 52750 Ocoyoacac, Estado de México, Mexico*

^c*ABACUS-Centro de Matemáticas Aplicadas y Cómputo de Alto Rendimiento, Departamento de Matemáticas, Centro de Investigación y de Estudios Avanzados (Cinvestav-IPN), Carretera México-Toluca km. 38.5, La Marquesa, 52740 Ocoyoacac, Estado de México, Mexico*

^d*Área de Física de Procesos Irreversibles, Departamento de Ciencias Básicas, Universidad Autónoma Metropolitana-Azcapotzalco (UAM-A), Av. San Pablo 180, 02200 México D.F., Mexico*

^e*EPHYSLAB (Environmental Physics Laboratory), Facultad de Ciencias, Campus de Ourense, Universidad de Vigo, 32004 Ourense, Spain*

Abstract

In this paper we implement a simple strategy, based on Jin and Braza's method, to deal with nonreflecting outlet boundary conditions for incompressible Navier-Stokes flows using the method of smoothed particle hydrodynamics (SPH). The outflow boundary conditions are implemented using an outflow zone downstream of the outlet, where particles are moved using an outgoing wave equation for the velocity field so that feedback noise from the outlet boundary is greatly reduced. For unidirectional flow across the outlet, this condition reduces to Orlanski's wave equation. The performance of the method is demonstrated through several two-dimensional test problems,

*Corresponding author

Email addresses: `iqcarlosug@gmail.com` (Carlos E. Alvarado-Rodríguez), `jaime.klapp@inin.gob.mx` (Jaime Klapp), `leonardo.sigalotti@gmail.com` (Leonardo Di G. Sigalotti), `jmdominguez@uvigo.es` (José M. Domínguez), `eduardo.delacruz@inin.gob.mx` (Eduardo de la Cruz Sánchez)

including unsteady, plane Poiseuille flow, flow between two inclined plates, the Kelvin-Helmholtz instability in a channel, and flow in a constricted conduit, and in three-dimensions for turbulent flow in a 90° section of a curved square pipe. The results show that spurious waves incident from the outlet are effectively absorbed and that steady-state laminar flows can be maintained for much longer times compared to periodic boundary conditions. In addition, time-dependent anisotropies in the flow, like fluid recirculations, are convected across the outlet in a very stable and accurate manner.

Keywords: Smoothed particle hydrodynamics (SPH); Boundary conditions; Open-boundary flows; Outflow; Flows in ducts, channels, nozzles, and conduits

1. Introduction

A standard procedure in engineering fluid dynamics for simulating internal flows is to artificially truncate their actual physical domain into a short region to reduce the computational cost. However, this demands the use of one or more open boundary conditions that must be specified at the extremes of the computational domain. Typical examples of this type of flows include pipe and channel flows, constricted flows in a pipe section, flows around bluff bodies, and external flows, in which case the flow develops in a practically infinite free stream, as in rising fire and hydrothermal seawater plumes, among others. Such open boundary conditions must allow the fluid to enter (inlet) and leave (outlet) the computational domain while reasonably minimizing non-physical feedbacks [1], such as the artificial build-up of fluid near the outlet [2] and the reflection of outgoing waves in recirculating flows at high and moderate Reynolds numbers [3]. In addition, numerical instabilities may well develop when strong vortices are convected through the outlet [4].

In this paper, we restrict ourselves to weakly compressible flows and introduce a practical methodology for handling nonreflecting outlet boundary conditions with smoothed particle hydrodynamics (SPH), when flow anisotropies are present near the outlet. Because of its Lagrangian character, SPH presents inherent disadvantages in the treatment of open boundary conditions compared to traditional Eulerian methods, where inlet and outlet boundary conditions for a stationary flow are more naturally described [2]. Earlier attempts of handling inlet/outlet boundaries with SPH for simple flows, such as Poiseuille and Couette flows, have been performed using

periodic boundary conditions [5]. In this case, the particle distribution is continually recycled so that any time a particle crosses the outlet, it is forced to re-enter the domain through the inlet. Although this interpolation has been widely employed in SPH simulations of internal, incompressible flows [6, 7, 8], it is known to degrade the numerical solution over time because disturbances in the particle distribution are re-introduced into the computational domain. For steady-state flows this problem is mitigated by just placing the outlet plane sufficiently far from the inlet to allow the numerical oscillations to be dissipated [9]. However, this may incur in an excessive increase of the computational burden.

A number of approaches has been presented in the literature to prescribe the correct inlet and outlet boundary conditions for weakly compressible and incompressible flows in SPH, with all of them aimed at reducing the level of disturbance at the outflow and therefore the reflections that may significantly alter the flow upstream. Truly incompressible SPH schemes (ISPH) employ a pressure-correction projection scheme to compute the pressure from a Poisson equation, which is then used to make the velocity field divergence-free [10, 11]. With these methods, solution of the Poisson equation typically requires implementing a homogeneous Neumann condition for the pressure [6, 12]. An improved algorithm, based on a non-homogeneous pressure boundary condition, the so-called rotational pressure-correction scheme [13], was implemented in ISPH by Hosseini and Feng [14]. Other strategies based on the use of a time-dependent driving force [15] and the influx of kinetic energy into the domain through the outflow boundaries [4] have also been designed.

On the other hand, weakly compressible SPH (WCSPH) solves the Navier-Stokes equations by defining the pressure through an algebraic relation so that the sound speed is artificially set to achieve accurate results in fluid propagation [16]. It is common practice in SPH to deal with spatially fixed (Eulerian) inlet and outlet boundaries by defining inflow and outflow regions that are external to the computational domain [5, 2, 9, 17]. These regions are filled with particles and their widths are comparable to or greater than the smoothing length of the fluid particles to avoid truncation of the kernel function. Thus, as a particle pertaining to the inflow region enters the fluid domain, a new one is automatically created to compensate it. According to the flow rates across the inlet and outlet, inflow and outflow particles are being added and removed, respectively. Here we describe a methodology, based on inflow and outflow zone particles, that conserves the global mass

of the system and minimizes the reflection of disturbances from the outlet back into the fluid domain. To this end, the velocity vector of particles in the outflow zone is evolved by means of an anisotropic propagation wave equation following the procedure described by Jin and Braza [18]. In addition to adapting their procedure for use in SPH simulations, the method is extended to three-space dimensions. We validate the method against several benchmark test cases for the simulation of two-dimensional (2D) internal flows, including unsteady, plane Poiseuille flow, flow along a divergent duct, the Kelvin-Helmholtz instability of flow with discontinuous shear in a channel, and plane choked flow through a constricted conduit. Validation of the method in three dimensions (3D) is shown against physical experiments for the turbulent flow in a 90° section of a curved square pipe.

2. WCSPH Formulation

For viscous incompressible flows, the governing equations are given by the Navier-Stokes equations

$$\frac{d\mathbf{v}}{dt} = -\frac{1}{\rho}\nabla p + \nu\nabla^2\mathbf{v}, \quad (1)$$

where ρ is the density, p the pressure, \mathbf{v} the velocity field, and ν the kinematic viscosity. In a WCSPH formulation, where the pressure is given as a function of the density, local variations of the pressure gradient may induce local density fluctuations in the flow. Therefore, the flow is modelled by an artificial fluid that is approximately incompressible. This is done by defining the total pressure gradient in Eq. (1) as [5]

$$-\frac{1}{\rho}\nabla p = -\frac{1}{\rho}\nabla p_d - \frac{1}{\rho}\nabla p_h = -\frac{1}{\rho}\nabla p_d + \mathbf{F}, \quad (2)$$

where p_d is the dynamical pressure as calculated from the equation of state, p_h is the hydrostatic pressure, and the term $-\nabla p_h/\rho$ is treated as a body force \mathbf{F} to be determined. In a WCSPH scheme, the mass of a fluid element remains constant and only its associated density fluctuates. Such density fluctuations are calculated by solving the continuity equation

$$\frac{d\rho}{dt} = -\rho\nabla \cdot \mathbf{v}. \quad (3)$$

The dynamical pressure p_d , which for simplicity we shall denote by p , is calculated using the relation [16]

$$p = p_0 \left[\left(\frac{\rho}{\rho_0} \right)^\gamma - 1 \right], \quad (4)$$

where $\gamma = 7$, $p_0 = c_0^2 \rho_0 / \gamma$, ρ_0 is a reference density, and c_0 is the sound speed at the reference density. This equation enforces very low density fluctuations since the speed of sound can be artificially slowed with accurate results in fluid propagation. By restricting the sound speed to be at least 10 times higher than the maximum expected fluid velocity, the density fluctuations will be within 1%.

In order to capture coherent turbulent structures within turbulent flows, the standard SPH viscous formulation is replaced by a sub-particle scaling (SPS) technique [19]. This is achieved by Favre-averaging Eqs. (1) and (3) over a length scale comparable to the particle sizes, where the velocity field \mathbf{v} can be decomposed into a mean part $\tilde{\mathbf{v}}$ and a fluctuating part \mathbf{v}' such that $\mathbf{v} = \tilde{\mathbf{v}} + \mathbf{v}'$, where the mean part is defined by a density weighted average, $\tilde{\mathbf{v}} = \overline{\rho \mathbf{v}} / \bar{\rho}$, and the overbars denote an arbitrary spatial filtering. Applying a flat-top spatial-filter to Eqs. (1) and (3), they become [20]

$$\frac{d\tilde{\mathbf{v}}}{dt} = -\frac{1}{\bar{\rho}} \nabla \bar{p} + \frac{\nu}{\bar{\rho}} [\nabla \cdot (\bar{\rho} \nabla)] \tilde{\mathbf{v}} + \frac{\nu}{\bar{\rho}} \nabla \cdot \mathbf{T}, \quad (5)$$

$$\frac{d\bar{\rho}}{dt} = -\bar{\rho} \nabla \cdot \tilde{\mathbf{v}}, \quad (6)$$

respectively, where \mathbf{T} is the SPS stress tensor defined in component form as

$$T_{ij} = \bar{\rho} \left(2\nu_t \tilde{S}_{ij} - \frac{2}{3} \tilde{S}_{kk} \delta_{ij} \right) - \frac{2}{3} \bar{\rho} C_I \Delta^2 \delta_{ij}, \quad (7)$$

where

$$\tilde{S}_{ij} = -\frac{1}{2} \left(\frac{\partial \tilde{v}_i}{\partial x_j} + \frac{\partial \tilde{v}_j}{\partial x_i} \right), \quad (8)$$

is the Favre-averaged strain rate tensor, $C_I = 0.00066$, $\nu_t = (C_s \Delta)^2 |\tilde{S}|$, with $C_s = 0.12$, is the Smagorinsky eddy viscosity, $|\tilde{S}| = (2\tilde{S}_{ij}\tilde{S}_{ij})^{1/2}$ is the local strain rate, δ_{ij} is the Kronecker delta, and Δ is a measure of the initial particle spacing.

3. SPH solver

The computer code used in this work is based on standard SPH methods [21, 22], where the density of particle a is given by the usual kernel summation

$$\rho_a = \sum_{b=1}^n m_b W_{ab}. \quad (9)$$

In this expression, m_b is the mass of particle b , $W_{ab} = W(|\mathbf{x}_a - \mathbf{x}_b|, h)$ is the kernel function, where $\mathbf{x}_a - \mathbf{x}_b$ is the distance between particles a and b and h is the width of the kernel or smoothing length, and the summation is taken over all n neighbour particles within the kernel support. Note that the density in Eq. (9) may be either the local density ρ or the particle-scale density $\bar{\rho}$ depending on whether we are dealing with laminar or turbulent (rotational) flows. The same is true for the velocity field, where \mathbf{v} may represent a local value (for laminar flows) or the Favre-averaged velocity $\tilde{\mathbf{v}}$ (for turbulent flows).

In Eqs. (1) and (5) the pressure gradient is written in SPH form using the symmetric representation proposed by Colagrossi and Landrini [23], which ensures numerical stability at the interface between two media with large density differences, while the laminar viscous term and the SPS stresses are discretized according to the formulations given by Lo and Shao [24]. Therefore, in SPH form Eq. (5) reads

$$\begin{aligned} \frac{d\mathbf{v}_a}{dt} = & - \frac{1}{\rho_a} \sum_{b=1}^n \frac{m_b}{\rho_b} (p_a + p_b) \nabla_a W_{ab} + 4\nu \sum_{b=1}^n m_b \frac{\mathbf{v}_a - \mathbf{v}_b}{\rho_a + \rho_b} \frac{\mathbf{x}_{ab} \cdot \nabla_a W_{ab}}{|\mathbf{x}_{ab}|^2 + \epsilon^2} \\ & + \sum_{b=1}^n m_b \left(\frac{\mathbf{T}_a}{\rho_a^2} + \frac{\mathbf{T}_b}{\rho_b^2} \right) \cdot \nabla_a W_{ab}, \end{aligned} \quad (10)$$

where $\mathbf{x}_{ab} = \mathbf{x}_a - \mathbf{x}_b$, $\epsilon^2 = 0.01h^2$, and W_{ab} is evaluated according to the symmetrized kernel function [25]

$$W_{ab} = \frac{1}{2} [W(|\mathbf{x}_a - \mathbf{x}_b|, h_a) + W(|\mathbf{x}_a - \mathbf{x}_b|, h_b)], \quad (11)$$

which has the correct limiting behaviour when $h_a = h_b$. For laminar flows the SPH representation of Eq. (1) can be recovered from the discrete Eq. (10) by dropping the SPS stress term and keeping in mind that the fluid

variables will now correspond to local quantities. Coupled to Eqs. (9) and (10), the equation

$$\frac{d\mathbf{x}_a}{dt} = \mathbf{v}_a + \frac{\beta}{M} \sum_{b=1}^N m_b \frac{\mathbf{x}_{ab}}{(\mathbf{x}_{ab} \cdot \mathbf{x}_{ab})^{3/2}} x_0 v_{\max}, \quad (12)$$

is solved for the particle positions, where the second term on the right-hand side is the shifting vector of particle a [26], which modifies the position of particles in order to prevent magnification of the SPH discretization errors due to anisotropies in their distribution. Here, β is a dimensionless parameter which is chosen to be $\beta = 0.04$, v_{\max} is the maximum velocity in the system, M is the total mass

$$M = \sum_{b=1}^N m_b, \quad (13)$$

and

$$x_0 = \frac{1}{N} \sum_{b=1}^N (\mathbf{x}_{ab} \cdot \mathbf{x}_{ab})^{1/2}. \quad (14)$$

Note that the summations in the above two expressions are over all particles filling the fluid domain. The addition of the shifting vector on the right-hand side of Eq. (12) does not affect momentum preservation.

Since direct evaluation of second-order derivatives of the kernel is not required, we adopt a low-order, Wendland C^2 function [27] as the interpolation kernel

$$W(q, h) = \frac{7}{4\pi h^2} \left(1 - \frac{q}{2}\right)^4 (2q + 1), \quad (15)$$

for $0 \leq q < 2$ and zero otherwise, where $q = |\mathbf{x} - \mathbf{x}'|/h$. A Verlet algorithm is used for the time integration of Eqs. (10) and (12), where the velocities and positions of particles are advanced from time t^n to time $t^{n+1} = t^n + \Delta t$ according to the difference formulae

$$\begin{aligned} \mathbf{v}_a^{n+1} &= \mathbf{v}_a^{n-1} + 2\Delta t \left(\frac{d\mathbf{v}_a}{dt}\right)^n, \\ \mathbf{x}_a^{n+1} &= \mathbf{x}_a^n + \Delta t \mathbf{v}_a^n + 0.5\Delta t^2 \left(\frac{d\mathbf{v}_a}{dt}\right)^n. \end{aligned} \quad (16)$$

In order to improve the coupling of Eqs. (10) and (12) during the entire evolution, the above time integration is replaced every 50 time steps by the

alternative difference forms

$$\begin{aligned}\mathbf{v}_a^{n+1} &= \mathbf{v}_a^n + \Delta t \left(\frac{d\mathbf{v}_a}{dt} \right)^n, \\ \mathbf{x}_a^{n+1} &= \mathbf{x}_a^n + \Delta t \mathbf{v}_a^n + 0.5 \Delta t^2 \left(\frac{d\mathbf{v}_a}{dt} \right)^n.\end{aligned}\quad (17)$$

This prevents the time integration to produce results that diverge from the actual solution. The time step, Δt , is calculated using the Courant-Friedrichs-Lewy (CFL) and the viscous diffusion conditions such that

$$\begin{aligned}\Delta t_{f,a} &= \min_a \left(h |dv_a/dt|^{-1} \right)^{1/2}, \\ \Delta t_{v,a} &= \max_b |h \mathbf{x}_{ab} \cdot \mathbf{v}_{ab} / (\mathbf{x}_{ab} \cdot \mathbf{x}_{ab} + \epsilon^2)|, \\ \Delta t_{cv,a} &= \min_a \left[h (c_a + \Delta t_{v,a})^{-1} \right], \\ \Delta t &= 0.3 \min_a (\Delta t_{f,a}, \Delta t_{cv,a}),\end{aligned}\quad (18)$$

where the maximum and minima are taken over all particles in the system, $v_a = (\mathbf{v}_{ab} \cdot \mathbf{v}_{ab})^{1/2}$, and c_a is the sound speed for particle a .

3.1. Solid boundary conditions

No-slip boundary conditions are implemented at contact with solid surfaces. A stable and accurate approach is achieved here using the method of image particles [5], where imaginary particles are initially created by simply reflecting actual fluid particles across the solid surface. Such particles are external to the fluid domain and serve to remove the kernel truncation in the proximity of the surface. Unlike actual fluid particles, imaginary particles are not allowed to move relative to the solid surface and are forced to maintain their initial distribution during the time evolution. However, a velocity needs to be assigned to each imaginary particle in order to evaluate the compressional and viscous forces in Eq. (10).

4. Inlet and outlet boundary conditions

We consider flow through a truncated section of a pipe, or channel, and assume that the open boundaries at the entrance and exit of the pipe section are perfectly planar. Since SPH particles cannot be spatially fixed at the

planar boundaries, we must allow them to flow in and out consistently with the flow rate across the inlet and outlet planes, respectively.

The method as presented here distinguishes among three zones, which are external to the computational domain, i.e., an inflow zone, which is placed in front of the pipe inlet, an outflow zone, which is placed downstream of the pipe exit plane, and a reservoir zone, where inert particles are temporarily stored. The inflow region consists of five columns of uniformly spaced particles and has a length equal to $5\Delta x_0$, where Δx_0 is the initial uniform spacing of the fluid particles in the direction of the flow. As in Refs. [5, 2, 14, 17], inflow particles are allowed to cross the inlet plane with a prescribed velocity that may vary in time and/or space. Scalar variables, such as density and pressure, are also prescribed for inflow particles. Since particles close to the inlet, but inside the flow domain, are updated according to Eqs. (9), (10), and (12), it always happens that some inflow particles that are close to the inlet fall within the kernel support of the near-boundary fluid particles. This will allow boundary information to be propagated into the flow domain [2].

The main differences between this and previously reported methods for WCSPH flows in SPH lie on the treatment of the outflow zone particles and the use of a reservoir buffer to ensure conservation of both the total mass and the total number of particles. The length of the outflow zone is chosen to be the same of the inflow zone. It is common practice to put this boundary sufficiently far from any sources of flow anisotropy, as may be the case of flow past a backward facing step, where the flow becomes essentially unidirectional and approaches a steady-state regime. In this case, classical “do-nothing” conditions [28, 29], where $d\mathbf{v}/dt = 0$ and

$$\mathbf{T} \cdot \mathbf{n} = 0, \tag{19}$$

at the outlet, have become the most widely used outflow conditions for the Navier-Stokes equations. Since these conditions are strictly valid for steady-state, fully-developed flows, they may present the problem of upstream wave propagation from the outlet if anisotropies are being convected into the outflow zone. An extension of the “do-nothing” conditions that enhances the stability properties against non-physical feedbacks has recently been proposed by Braack and Mucha [30].

Here we implement a type of outflow boundary condition that simulates the propagation of waves out of the computational domain by allowing the flow to cross the outlet without being significantly reflected back. To do so

we adopt the procedure described in Ref. [18], which is based on a wave equation and allows for anisotropic wave propagation across the outlet. The velocity vector of particles crossing the outlet and entering the outflow zone is considered as a transported wave quantity incident on the boundary. To this end, we consider the wave equation

$$\frac{\partial^2 \mathbf{v}}{\partial t^2} - c_x^2 \frac{\partial^2 \mathbf{v}}{\partial x^2} - c_y^2 \frac{\partial^2 \mathbf{v}}{\partial y^2} - c_z^2 \frac{\partial^2 \mathbf{v}}{\partial z^2} = \mathbf{0}, \quad (20)$$

where c_x , c_y , and c_z are the characteristic velocities of wave propagation in the x -, y -, and z -directions, respectively. Introducing the differential operator \mathcal{L} as

$$\mathcal{L} = c_x^2 \frac{\partial^2}{\partial x^2} + c_y^2 \frac{\partial^2}{\partial y^2} + c_z^2 \frac{\partial^2}{\partial z^2} - \frac{\partial^2}{\partial t^2}, \quad (21)$$

Eq. (20) can be rewritten as

$$\mathcal{L} \mathbf{v} = \mathcal{L}^+ \mathcal{L}^- \mathbf{v} = \mathbf{0}, \quad (22)$$

where \mathcal{L}^+ and \mathcal{L}^- are factorization operators providing information on the outgoing and ingoing (reflected) waves, respectively. The decomposition of \mathcal{L} into the product $\mathcal{L}^+ \mathcal{L}^-$ yields the forms

$$\mathcal{L}^+ = c_x \frac{\partial}{\partial x} + \frac{\partial}{\partial t} (1 - s^2)^{1/2}, \quad (23)$$

$$\mathcal{L}^- = c_x \frac{\partial}{\partial x} - \frac{\partial}{\partial t} (1 - s^2)^{1/2}, \quad (24)$$

where

$$s^2 = c_y^2 \left(\frac{\partial}{\partial y} \right)^2 \left(\frac{\partial}{\partial t} \right)^{-2} + c_z^2 \left(\frac{\partial}{\partial z} \right)^2 \left(\frac{\partial}{\partial t} \right)^{-2}. \quad (25)$$

Application of the equation $\mathcal{L}^- \mathbf{v} = \mathbf{0}$ to the outflow particles results in a total non-reflecting condition. Now, using the approximation $(1 - s^2)^{1/2} \approx 1 - s^2/2$ for s small and making $c_y \approx c_z = c$, gives for the outgoing wave

$$\frac{\partial \mathbf{v}}{\partial t} + c_x \frac{\partial \mathbf{v}}{\partial x} - \frac{1}{2} c^2 \left(\frac{\partial}{\partial t} \right)^{-1} \left(\frac{\partial^2 \mathbf{v}}{\partial y^2} + \frac{\partial^2 \mathbf{v}}{\partial z^2} \right) = \mathbf{0}, \quad (26)$$

where the anisotropic term containing the coefficient c is a diffusion-like term. Noting that $c^2(\partial/\partial t)^{-1}$ has the same dimensions of the kinematic viscosity ν , a matching of Eq. (26) with the Navier-Stokes equations can be made

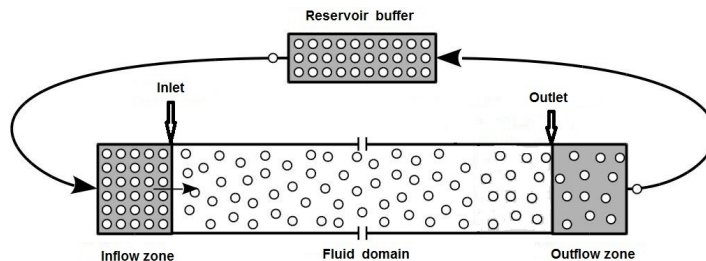


Figure 1: Schematic drawing of the inflow, outflow, and reservoir zones. When an inflow particle enters the fluid domain, a reservoir particle is automatically inserted in the first layer of inflow particles. Similarly, when a particle leaves the outflow zone it is temporarily stored in the reservoir buffer.

by applying the following equivalences $2\nu \rightarrow c^2(\partial/\partial t)^{-1}$ and $c_x \rightarrow v_x$, where v_x is the x -component of the velocity field. In this way, the outgoing wave equation becomes

$$\frac{\partial \mathbf{v}}{\partial t} + v_x \frac{\partial \mathbf{v}}{\partial x} - \nu \left(\frac{\partial^2 \mathbf{v}}{\partial y^2} + \frac{\partial^2 \mathbf{v}}{\partial z^2} \right) = \mathbf{0}, \quad (27)$$

where $\mathbf{v} = (v_x, v_y, v_z)$. If the diffusion term is dropped, Eq. (27) reduces to

$$\frac{\partial \mathbf{v}}{\partial t} + v_x \frac{\partial \mathbf{v}}{\partial x} = \mathbf{0}, \quad (28)$$

which is the Orlandi equation for unidirectional monochromatic travelling waves [31]. Note that setting $\mathbf{v} = (v_x, v_y)$ with v_x and v_y depending only on x and y , Eq. (27) reduces to the 2D form derived by Jin and Braza [18].

Particles in the outflow zone are evolved using either Eq. (27) or (28) until they flow past its downstream limit. When a particle leaves the outflow zone its velocity is automatically zeroed and it is temporarily stored in a reservoir buffer. Figure 1 shows a schematic diagram of the inflow and outflow

boundary zones. Every time an inflow particle enters the fluid domain, a particle is removed from the reservoir buffer and inserted in the upstream side of the inflow zone with the desired prescribed velocity and density. This is a necessary step because in most problems of interest the inlet and outlet mass rates and cross-sections may differ. At the beginning of a calculation the number of reservoir particles depends on the flow model and can be as large as needed.

In SPH form Eq. (27) for an outflow zone particle “o” is written as follows

$$\begin{aligned} \frac{\partial \mathbf{v}_o}{\partial t} &= -v_{x,o} \sum_{b=1}^n \frac{m_b}{\bar{\rho}_{ob}} (\mathbf{v}_b - \mathbf{v}_o) \frac{\partial W_{ob}}{\partial x_o} \\ &+ 2\nu \sum_{b=1}^n \frac{m_b}{\rho_b} \frac{(\mathbf{v}_b - \mathbf{v}_o)}{|\mathbf{x}_{ob}|^2 + \epsilon^2} \left(y_{ob} \frac{\partial W_{ob}}{\partial y_o} + z_{ob} \frac{\partial W_{ob}}{\partial z_o} \right), \end{aligned} \quad (29)$$

where $\mathbf{x}_{ob} = \mathbf{x}_o - \mathbf{x}_b$, $y_{ob} = y_o - y_b$, and $z_{ob} = z_o - z_b$. Flow particles next to the outlet plane are updated according to the usual SPH procedures so that some outflow particles may fall inside the compact support of the near-boundary fluid particles. The same is true for outflow particles close to the outlet in Eq. (29) where some neighbours b may actually be fluid particles, allowing fluid information to be propagated into the outflow zone. In order to ensure stability of Eq. (29), the velocity $v_{x,o}$ is smoothed according to

$$v_{x,o} = \sum_{b=1}^n \frac{m_b}{\rho_b} v_{x,b} W_{ob}, \quad (30)$$

where the summation is taken over all neighbours of outflow zone particle “o”. This is, in fact, equivalent to averaging the convective velocity at the outlet. The position of outflow particles is updated according to $d\mathbf{x}_o/dt = \mathbf{v}_o$, which together with Eq. (29), is integrated in time using the Verlet algorithm described by Eqs. (16) and (17).

5. Numerical tests

5.1. Unsteady plane Poiseuille flow

As a first test we consider the Poiseuille flow between stationary infinite plates placed at distances $y = \pm 5 \times 10^{-4}$ m from the centre $y = 0$. For this test, the Navier-Stokes equations admit the exact solution

$$v_x(y, t) = \frac{F}{2\nu} (y^2 - d^2)$$

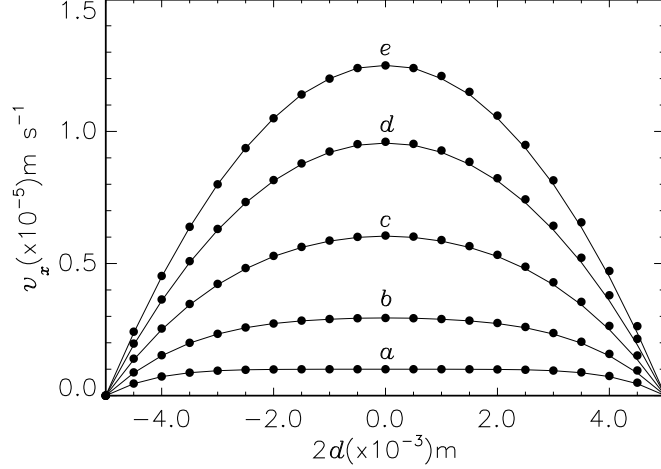


Figure 2: SPH velocity profiles using the nonreflecting outlet boundary condition (dots) as compared with the analytical solution (solid lines) for unsteady plane Poiseuille flow with Reynolds number, $Re=0.0125$, at: (a) 0.01 s, (b) 0.03 s, (c) 0.07 s, (d) 0.15 s, and (e) 1.0 s. A steady-state profile is already obtained at about 1.0 s.

$$+ \sum_{n=0}^{\infty} \frac{16(-1)^n d^2 F}{\nu \pi^3 (2n+1)^3} \cos \left[\frac{(2n+1)\pi y}{2d} \right] \exp \left[-\frac{(2n+1)^2 \pi^2 \nu t}{4d^2} \right] \quad (31)$$

where d is half the distance between the parallel plates, $\nu = \eta/\rho$ is the kinematic viscosity, and $F = -2\nu v_0/d^2$ is a driving force proportional to the pressure difference (Δp) between the inlet and outlet, and $v_0 = -d^2 \Delta p / (2\rho \nu L)$ is a constant asymptotic velocity, where L is the length of the pipe section. In the limit when $t \rightarrow \infty$ the above solution tends to the well-known steady-state, parabolic profile

$$v_x(y) = v_0 \left(1 - \frac{y^2}{d^2} \right). \quad (32)$$

For this test problem we choose $\rho_0 = 1000 \text{ kg m}^{-3}$, $v_0 = 1.25 \times 10^{-5} \text{ m s}^{-1}$, and $\nu = 1.0 \times 10^{-6} \text{ m}^2 \text{ s}^{-1}$, corresponding to a Reynolds number $Re = 2dv_0/\nu = 0.0125$. The fluid domain is filled with 1942 particles initially at rest and regularly distributed in the spanwise direction between $x = 0$ and $x = L = 2.33 \times 10^{-4} \text{ m}$. The particles are given a smoothing length $h \approx 2.4 \times 10^{-5} \text{ m}$ and Eq. (4) is used as the pressure-density relation with $c_0 = 2 \text{ m s}^{-1}$.

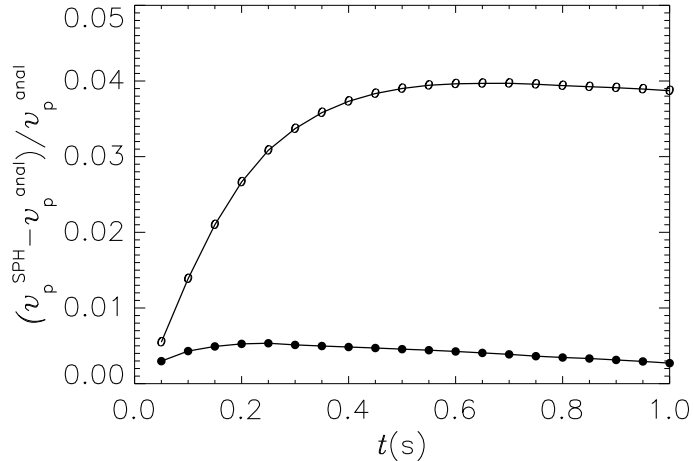


Figure 3: Relative error of the SPH peak velocity, v_p^{SPH} , as compared with the theoretically predicted value, v_p^{anal} , as a function of time. The dots correspond to the calculation of Fig. 2 with nonreflecting outlet boundary conditions. For comparison, the circles represent the resulting relative errors when periodic boundary conditions are used for the same test.

The transient behaviour as calculated with the outlet boundary condition treatment is shown in Fig. 2, where the SPH solution (dots) is compared with the theoretically predicted one (solid lines) at selected times. The solution is depicted up to $t = 1.0$ s when a steady-state regime has been already established. Figure 3 shows the relative errors between the numerical and analytical peak velocities for the run of Fig. 2 with the outflow boundary condition method (dots) as compared with an identical run using periodic boundary conditions (circles). The error in the periodic simulation grows rapidly during the first 0.4 s and reaches values that are an order of magnitude greater than the error carried by the nonreflecting outlet simulation. This difference is the result of cumulative errors due to the recycling of numerical disturbances in the periodic simulation. Figure 4 also shows the numerical y -component of the velocity for both calculations. With the present method (top frame), the numerically induced y -component of the velocity reaches maximum absolute values above and below $y = 0$ of $\approx 4.0 \times 10^{-14}$ m s $^{-1}$, while in the periodic case (bottom frame) v_y exhibits erratic oscillations after ~ 0.4 s and reaches values that are about 7 orders of magnitude higher. The asymmetry of the oscillations with respect to the central plane $y = 0$ is

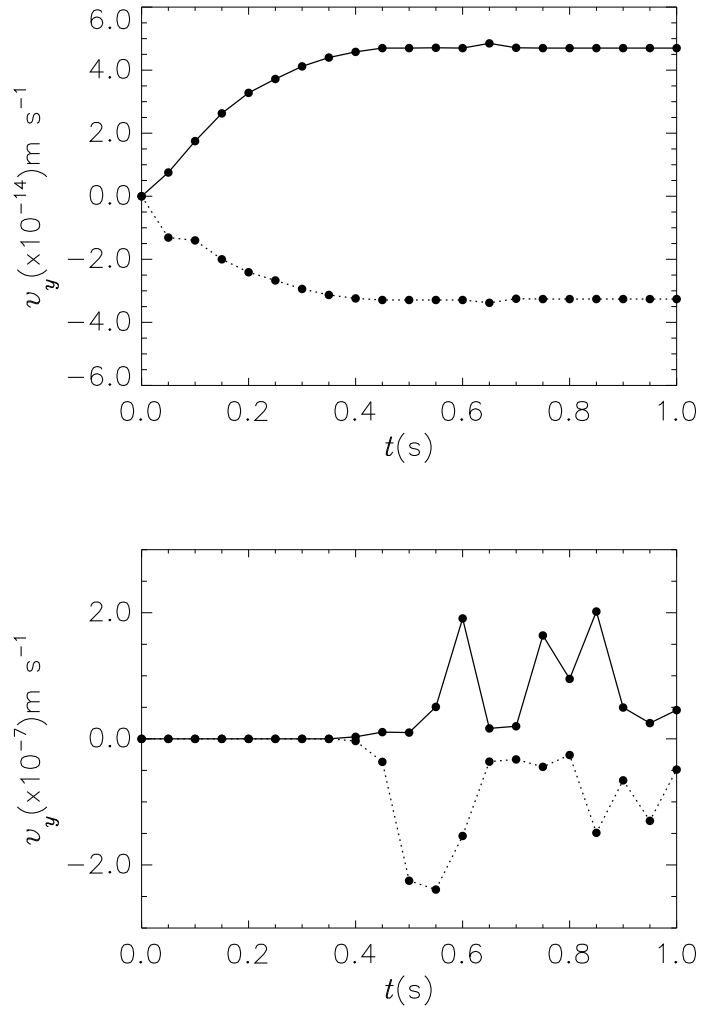


Figure 4: Maximum values of the numerically induced y -component of the velocity above (dotted-solid line) and below (dotted-dashed line) the central plane ($y = 0$) as a function of time for the plane Poiseuille flow of Fig. 2 using nonreflecting outlet (top frame) and periodic boundary conditions (bottom frame). The level of anisotropy is about seven orders of magnitude lower for the nonreflecting outlet simulation.

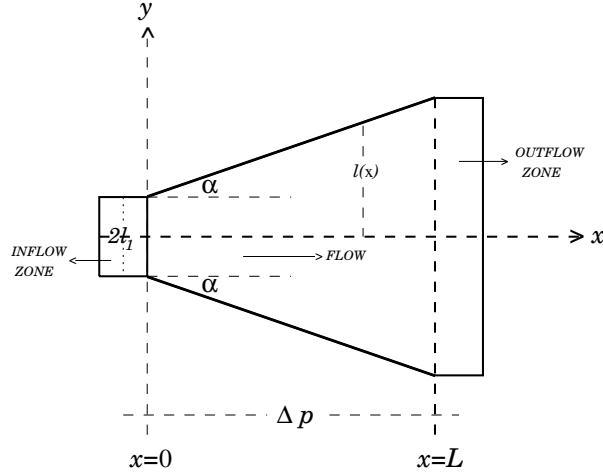


Figure 5: Top view of the flow geometry between two inclined plates.

indicative of the presence of noise due to the periodic recycling of particles. Evidently, the nonreflecting outlet boundary conditions are doing a superior job for this test as the flow remains laminar with a very good accuracy.

5.2. Flow between inclined plates

As a second test, we consider the case of laminar flow between two inclined plates, where the inlet and outlet cross-sections differ as shown in Fig. 5. If the inclination angle α is small and the flow is driven by a pressure difference between the inlet and outlet planes, an analytical solution can be derived for the streamwise velocity after a steady-state flow is reached [32, 33], namely

$$v_x = -\frac{\Delta p}{\eta L} \left[y^2 - (l_1 + x \tan \alpha)^2 \right] \frac{l_1^2 (l_1 + L \tan \alpha)^2}{(2l_1 + L \tan \alpha) (l_1 + x \tan \alpha)^3}, \quad (33)$$

where $\eta = \rho\nu$ is the shear viscosity, l_1 is half the separation of the inclined plates at the inlet, and L is the distance between the inlet and outlet planes. Following the procedure described by Liang et al. [33], the body force at the

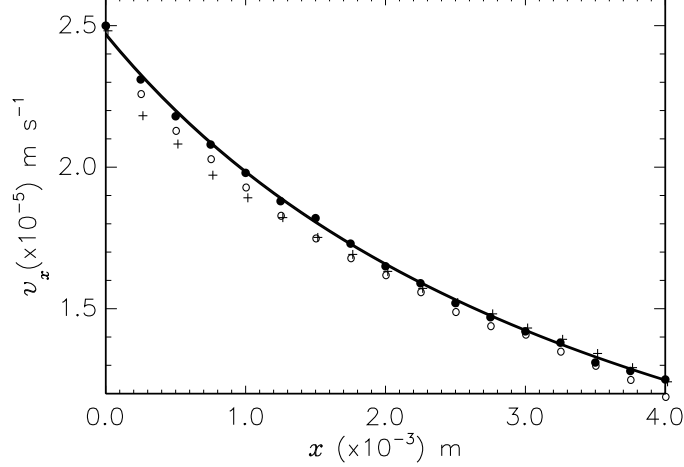


Figure 6: Steady-state streamwise velocity profile as a function of position along the inclined plates. The analytical solution given by Eq. (33) (solid line) is compared with the numerically obtained profiles at different spatial resolutions: $N = 6592$ (crosses), 15984 (circles), and 103168 (dots).

inlet $x = 0$ is given by

$$F(x = 0) = \frac{2\Delta p \tan \alpha}{\rho l_1^3} \left[\frac{1}{(l_1 + L \tan \alpha)^2} - \frac{1}{l_1^2} \right]^{-1}, \quad (34)$$

while at any streamwise position x it obeys the relation

$$F(x) = \left[\frac{l_1}{l(x)} \right]^3 F(x = 0), \quad (35)$$

where $l(x) = l_1 + x \tan \alpha$. This gives $F(x = L) = F(x = 0)/(1 + L \tan \alpha/l_1)^3$ at the outlet. Equations (33)–(35) are valid if the Reynolds number $\text{Re} < 1$ and $L \gg l_1$.

For this test case we choose the same parameters as in Liang et al. [33], that is, $\Delta p \approx -1.217 \times 10^{-3} \text{ N m}^{-2}$, $L = 4 \text{ mm}$, $2l_1 = 0.5 \text{ mm}$, $\nu = 1.0 \times 10^{-6} \text{ m}^2 \text{ s}^{-1}$, $\rho = 1000 \text{ kg m}^{-3}$, and $\alpha = 3.503^\circ$, except for the sound speed which is taken to be $c = 5.0 \text{ m s}^{-1}$ in order to keep the density fluctuations below 1% with the use of Eq. (4). In contrast, Liang et al. [33] used an equation of state of the form $p = c^2 \rho$ with $c = 2.5 \times 10^{-4} \text{ m s}^{-1}$. Initially the particles are

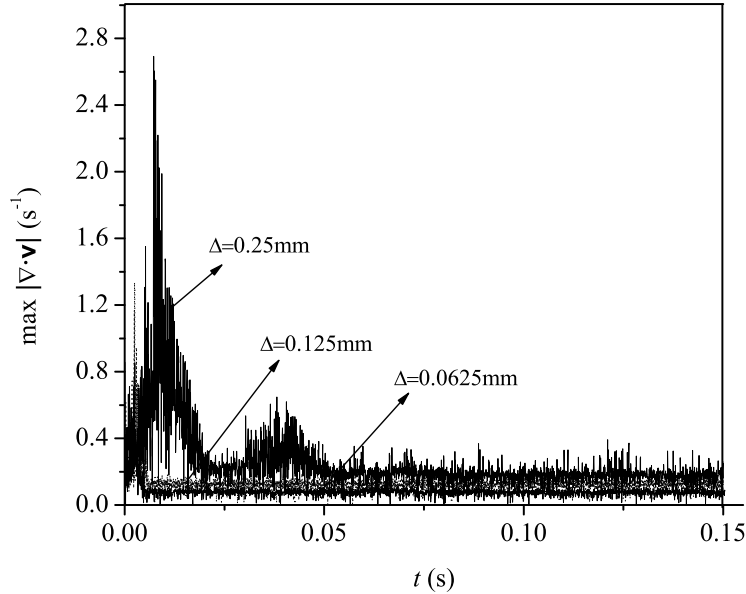


Figure 7: Absolute value of the maximum divergence of the velocity field as a function of time for flow between two inclined plates. The results for the three resolutions tried are shown.

at rest and distributed on a regular Cartesian mesh and the initial smoothing length is set to $h = 1.1\Delta$, where Δ is the initial interparticle distance along the x - and y -directions. With the above parameters, the Reynolds number of the flow is $\text{Re} = 2l_1v_0/\nu = 0.0125$, where $v_0 = 2.5 \times 10^{-5} \text{ m s}^{-1}$ is the velocity at the inlet plane. According to Eq. (34), the body force at the inlet is $F(x = 0) = 8.0 \times 10^{-4} \text{ m s}^{-2}$, while the body force entering in Eq. (2) is $\mathbf{F} = \mathbf{x}F(x)$, which is always parallel to the x -axis and zero otherwise.

Figure 6 depicts the x -component of the fluid velocity after about 0.15 s when the flow reaches a steady state. The numerically obtained profiles are compared with the analytical solution (solid line) as given by Eq. (33). Three different runs are shown with identical initial parameters but varied initial spatial resolution: $N = 6592$ (crosses), 15984 (circles), and 103168 (dots), corresponding to initial interparticle separations of 0.25, 0.125, and 0.0625 mm, respectively. Figure 6 shows that the results obtained with the present method converge to the theoretical solution as the resolution is increased. In

terms of the root-mean-square error (RMSE)

$$\text{RMSE}(v_x) = \sqrt{\frac{1}{N} \sum_{a=1}^N (v_{x,a}^{\text{anal}} - v_{x,a}^{\text{SPH}})^2}, \quad (36)$$

where $v_{x,a}^{\text{anal}}$ represents the analytical solution (33) at the position of particle a and $v_{x,a}^{\text{SPH}}$ the corresponding SPH calculated value, the numerical errors decrease with decreasing initial particle size with $\text{RMSE}(v_x) \approx 1.49 \times 10^{-6} \text{ m s}^{-1}$ (for $\Delta = 0.25 \text{ mm}$), $\approx 1.06 \times 10^{-6} \text{ m s}^{-1}$ (for $\Delta = 0.125 \text{ mm}$), and $\approx 1.54 \times 10^{-7} \text{ m s}^{-1}$ (for $\Delta = 0.0625 \text{ mm}$).

The pressure constant p_0 in Eq. (4) governs the relative density fluctuations $|\Delta\rho|/\rho_0$, with $\Delta\rho = \rho - \rho_0$. Since $|\Delta\rho|/\rho_0 \sim M^2$, where M is the Mach number, density fluctuations in the flow can be kept of the order of 1%, or less, by choosing $M \leq 0.1$. To enforce this condition p_0 must be equal to $c_0^2\rho_0/\gamma$, where c_0 is the sound speed at the reference density ρ_0 which is chosen large enough to guarantee that $M \leq 0.1$. Figure 7 shows the maximum value of $|\nabla \cdot \mathbf{v}|$ in the flow as a function of time for the three resolutions tried. During the first 0.05 s, peaks of the velocity divergence as high as $\sim 2.7 \text{ s}^{-1}$ and $\sim 0.6 \text{ s}^{-1}$ arise in the low resolution run. At later times, the maximum velocity divergence decreases and oscillates about 0.2 s^{-1} . As the resolution is increased to $\Delta = 0.1250 \text{ mm}$, the peak intensity at the beginning is reduced to less than $\sim 0.8 \text{ s}^{-1}$ and the maximum value of the divergence oscillates about $\sim 0.12 \text{ s}^{-1}$. This mean value improves to $\sim 0.08 \text{ s}^{-1}$ for the high resolution run. In this case, the divergence achieves a peak of $\sim 0.4 \text{ s}^{-1}$ at the very beginning. The actual maximum density fluctuations associated with these deviations from exact incompressibility (calculated as the product $\max(|\nabla \cdot \mathbf{v}|_a)\Delta t$) correspond to mean values of 3.2×10^{-7} (for $\Delta = 0.25 \text{ mm}$), 2.6×10^{-7} (for $\Delta = 0.125 \text{ mm}$), and 9.1×10^{-8} (for $\Delta = 0.0625 \text{ mm}$).

5.3. Kelvin-Helmholtz instability in a channel

We now assess the ability of our method to inhibit feedback noises when convecting flow anisotropies across the outlet. The test case concerns the onset of the Kelvin-Helmholtz (KH) instability at the interface between two shearing fluids of different velocities when velocity perturbations perpendicular to the interface grow to eventually mix the layers [34]. We consider a two-dimensional setup similar to that reported by Price [35], using $N = 10880$ equal mass particles filling the domain $0 \leq x \leq 0.4 \text{ m}$ and $0 \leq y \leq 0.1442$

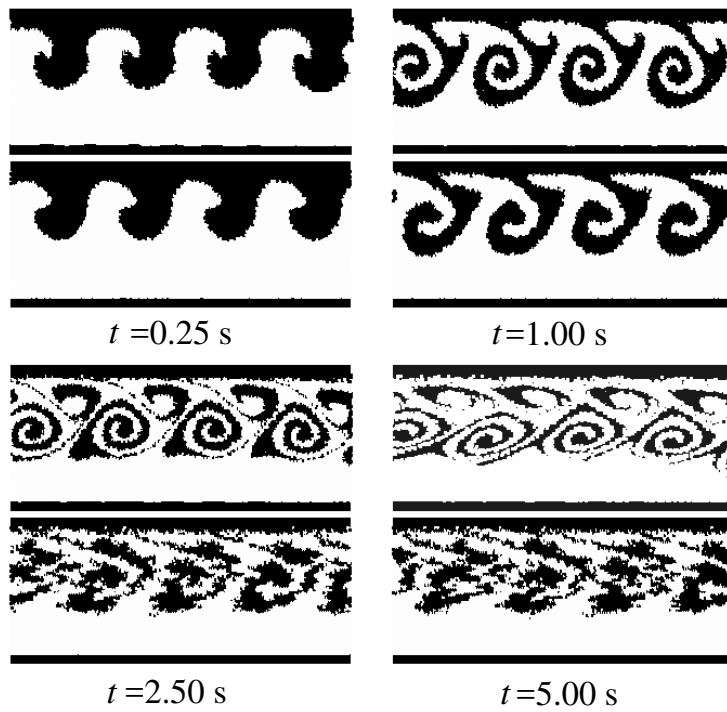


Figure 8: Density maps of the two-dimensional KH instability at different times. At each time, the top and bottom frames correspond to identical simulations using the nonreflecting outlet and periodic boundary conditions in the x -direction, respectively. Except for small features, the linear and early non-linear growth is similar in both simulations up to about 1.0 s.

m. The particles are initially placed on a uniform Cartesian array and the density is set to $\rho = 1000 \text{ kg m}^{-3}$ everywhere.

A shear flow is setup in the x -direction with velocity $v_x = 1 \text{ m s}^{-1}$ for $0 \leq y < 0.103 \text{ m}$ and $v_x = 2 \text{ m s}^{-1}$ for $0.103 \leq y \leq 0.1442 \text{ m}$, so that the tangential fluid velocity has a discontinuous jump across the interface between the streams. This flow corresponds to $\text{Re} = 10000$. For this test we use Eq. (4) with $c_0 = 40 \text{ m s}^{-1}$. This configuration is known to be susceptible to a KH instability at all wavelengths. The instability is seeded by introducing a small velocity in the y -direction given by

$$v_y = A \sin \left[\frac{-2\pi}{\lambda} \left(x + \frac{1}{2} \right) \right], \quad (37)$$

for $0.09 < y < 0.116 \text{ m}$ and zero elsewhere, with $A = 0.5 \text{ m s}^{-1}$ and $\lambda = 0.1 \text{ m}$. For this setup the linear KH growth time-scale for the sinusoidal mode defined by

$$\tau_{\text{KH}} = \frac{2\lambda}{|v_{x,1} - v_{x,2}|}, \quad (38)$$

is $\tau_{\text{KH}} = 0.2 \text{ s}$. No-slip boundary conditions are applied at contact with the walls of the channel. For this test the inlet consists of an upstream section of 0.8 m long, while the actual channel has a length of 0.4 m and the out-flow zone is 0.1 m long. Initially, the inlet and the channel sections are filled with particles, which are then evolved from the above initial conditions using SPH. As the flow proceeds, the inlet section becomes progressively depleted of particles, resembling a moving piston boundary condition. The calculation is halted immediately before the inlet becomes completely depleted of particles. At the exit of the channel, the outlet boundary conditions are employed. For this test calculation, Eq. (5) is used with the viscous force term replaced by an artificial viscosity using the scheme proposed by Monaghan [21] with a coefficient $\alpha_\nu = 0.01$. In order to test the performance of the non-reflecting outlet boundary conditions, a second run using periodic boundary conditions at the inlet and outlet in the x -direction was performed for direct comparison. Figure 8 shows the results at different times up to 5.0 s . At each time, the top and bottom frames correspond to nonreflecting outlet and periodic simulations, respectively. In the former case 5508 inflow particles were needed to follow the evolution up to 5.0 s by which time the inflow zone was almost depleted. With the nonreflecting boundary conditions the linear growth phase is similar to the periodic simulation. The instability grows at

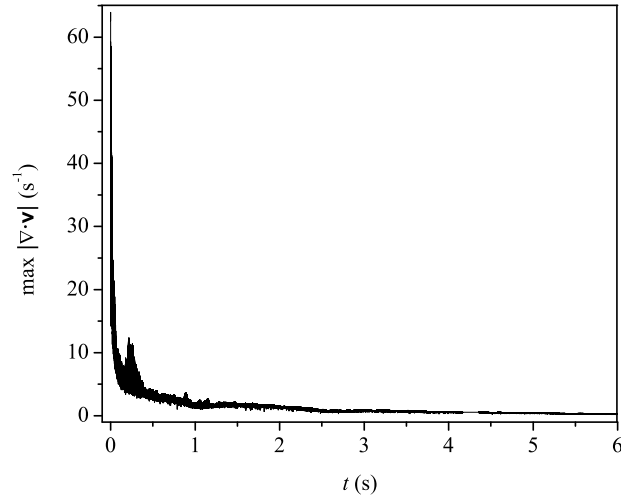


Figure 9: Absolute value of the maximum velocity divergence as a function of time for the KH instability simulation of Fig. 8 using nonreflecting outlet boundary conditions.

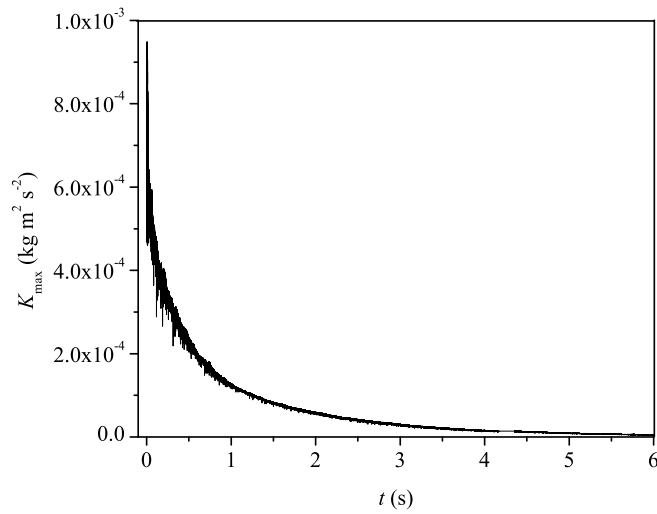


Figure 10: Maximum value of the kinetic energy as a function of time for the KH instability simulation of Fig. 8 using nonreflecting outlet boundary conditions.

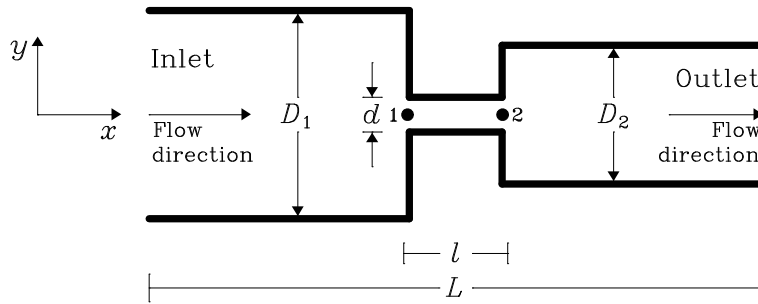


Figure 11: Top view of the constricted channel section for choked flow.

the shear layer and the peaks of each fluid phase penetrate into each other ($t = 0.25$ s). After further penetration of the fluid phases, non-linear shear leads them to roll up into the well-known KH whorls ($t = 1.0$ s). We may see that the whorl height is nearly identical in both calculations. However, at $t = 1.0$ s the rolling appears to be slightly more pronounced in the nonreflecting outlet simulation. At later times, the interface rolls up into a sequence of spiral vortices ($t = 2.5$ s). As time progresses, the turns are elliptically deformed ($t = 5.0$ s). While a vortex field is formed with the nonreflecting boundary conditions, which then amplifies and eventually leads to mixing, the solution with periodic boundary conditions looks highly degraded by $t = 2.5$ s because of the continued re-entry of numerical perturbations.

Figure 9 depicts the time evolution of the absolute value of the maximum velocity divergence for the nonreflecting outlet simulation. At the very beginning the velocity divergence drops sharply, decaying from $\sim 67 \text{ s}^{-1}$ to less than $\sim 0.3 \text{ s}^{-1}$ during the first second of the evolution. After this time, it decreases slowly to less than $\sim 0.2 \text{ s}^{-1}$ by $t = 6.0$ s. In addition, Fig. 10 shows the time evolution of the maximum kinetic energy. During the first two seconds, the maximum kinetic energy is seen to decrease rapidly by an order of magnitude and then at a much slower rate during the spiraling and elliptical deformation of the vortex sheet, reaching a value of $\sim 4.0 \times 10^{-6} \text{ kg m}^2 \text{ s}^{-2}$ by 6.0 s, when the calculation is terminated because of particle depletion in the inlet section.

5.4. Flow through a constricted channel

As a further test we consider the flow between two parallel walls with a sharp-edged, narrow passage (or throat) of length l at the centre of the channel, as shown in the top view of Fig. 11. The main flow direction is taken

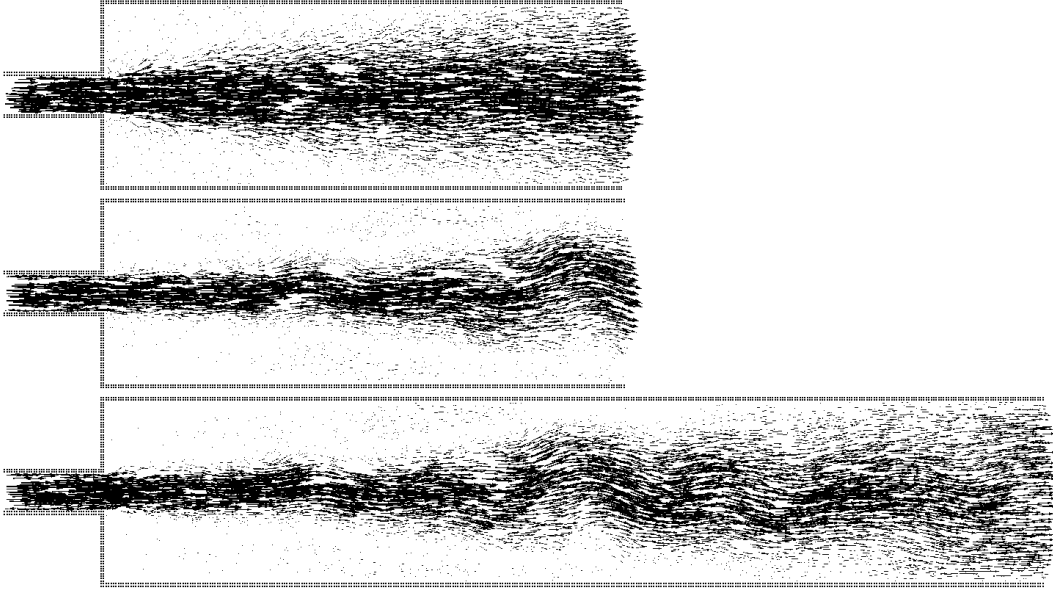


Figure 12: Velocity vectors in the throat and downstream sections of the channel at $t = 4.65$ s for three separate simulations: the R1 run using an Orlandi type outlet boundary condition with no anisotropic term in Eq. (29) (top frame), the R2 run with the anisotropic term in Eq. (29) included (middle frame), and the R3 run, which is identical to R2 but with a longer downstream section (bottom frame). A very good agreement for R2 and R3 is shown, proving the efficiency of the nonreflecting type boundary conditions implemented by solving the outgoing wave Eq. (29).

along the x -axis and the depth of the channel is assumed to be infinite so that the flow is in the (x,y) -plane. Three separate simulations are considered. Two of them use identical parameters except that in one run (R1) particles in the outflow zone are evolved solving Eq. (29) with the anisotropic term dropped to mimic an Orlandi type outlet boundary condition, while the second run (R2) solves Eq. (29) including the anisotropic term. A third run (R3) is identical to R2 but with a longer downstream pipe section. This test problem is more stringent than the previous examples because downstream the throat anisotropic flow develops as in the case of flow past a backward facing step. In addition, if the throat is modelled as a very narrow passage, its cross-section can be made to strongly differ from that of the outlet as desired.

For these simulations we take $\rho = 1000 \text{ kg m}^{-3}$, $\nu = 1.0 \times 10^{-6} \text{ m}^2 \text{ s}^{-1}$, and a time-varying plane Poiseuille velocity profile in the inflow zone given

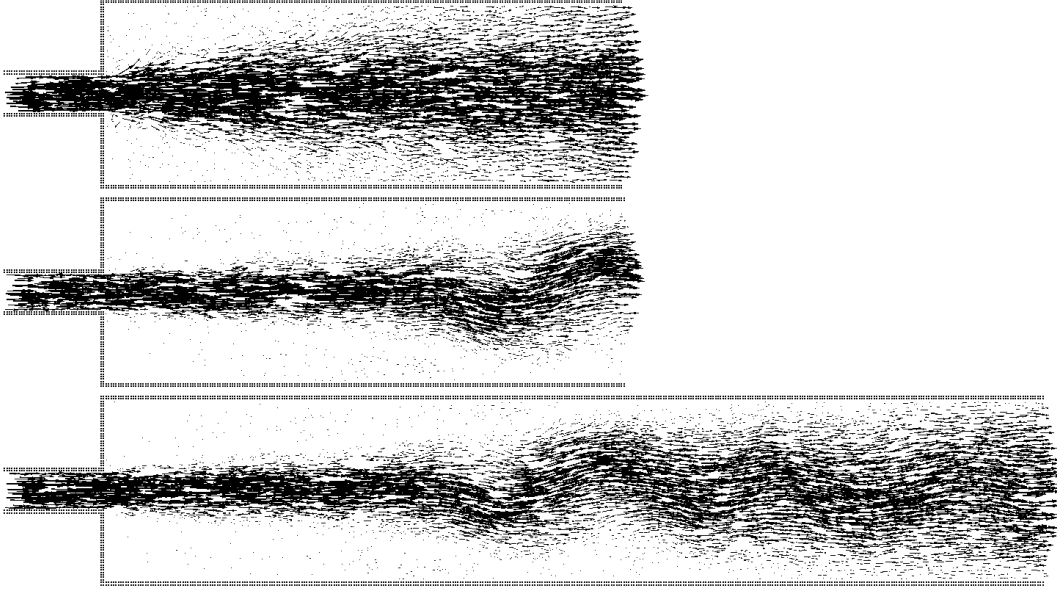


Figure 13: The same as Fig. 12 but at $t = 6.0$ s.

by

$$v_{\text{in}} = v_0 \left(\frac{t}{t_0} \right) \left(1 - \frac{4y^2}{D_1^2} \right), \quad (39)$$

where $t_0 = 0.2$ s and $v_0 = 4.45 \times 10^{-2}$ m s $^{-1}$. The inlet flow is exactly zero at $t = 0$ and increases linearly with time in the course of the evolution. This is equivalent to applying a pressure difference by suction on the outlet. When $t \geq t_0$, we set $t/t_0 = 1$ and the inlet flow becomes time-independent. The sound speed is taken to be $c_0 = 1.0$ m s $^{-1}$ and Eq. (4) is used as the pressure-density relation. The throat has a length of $l = 7.78$ cm and an opening width of $d \approx 1.33$ cm. The upstream section has a width of $D_1 \approx 8.89$ cm and a length $l_1 = 20$ cm, while the downstream section has a width of $D_2 \approx 7.56$ cm and a length $l_2 = 20$ cm for models R1 and R2 and $l_2 = 36$ cm for model R3. For these simulations we use a total of 37467 (for models R1 and R2) and 50346 regularly distributed particles (for model R3) filling the entire channel.

The influence of the computational domain size and type of nonreflecting boundary conditions as given by Eqs. (27) and (28) are now examined. Figures 12 and 13 display the velocity field in the throat and downstream sections at $t = 4.65$ and 6.0 s, respectively. The top frame shows the flow

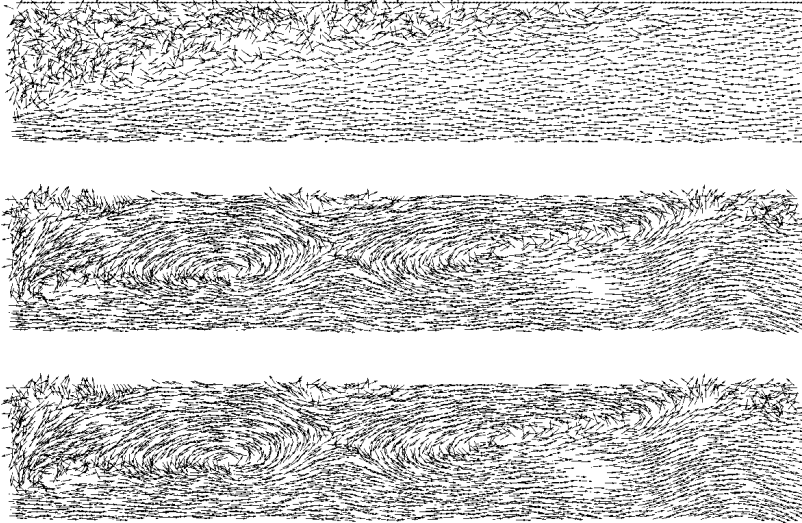


Figure 14: Blowup view of the downstream section showing details of the flow on the side just above the vena contracta at $t = 4.65$ s for the three models of Fig. 12. To facilitate direct comparison, the length of the downstream section used for models R1 (top frame) and R2 (middle frame) is also shown for model R3 (bottom frame).

structure for model R1 with the Orlanski type outlet boundary, while the other two frames correspond to models R2 (middle frame) and R3 (bottom frame) using nonreflecting conditions with the anisotropic term in Eq. (29) included and a different size of the downstream section. The Reynolds number in the throat conduit can be defined as $Re = v_m d / \nu$, where v_m is the mean velocity there. This gives $Re \approx 4531$ (at $t = 4.65$ s) and ≈ 4552 (at $t = 6.0$ s) for cases R2 and R3, while $Re \approx 4516$ (at $t = 4.65$ s) and $Re \approx 4546$ (at $t = 6.0$ s) for model R1. At $t = 6.0$ s, the maximum velocity at the exit of the throat is $v_{max} \approx 0.43$ m s⁻¹ for model R1 against $v_{max} \approx 0.40$ m s⁻¹ for models R2 and R3, while the mean pressure drop through the throat is $\Delta p \approx 6.51 \times 10^{-3}$ Pa for model R1 compared to $\Delta p \approx 1.22 \times 10^{-2}$ Pa for the other two cases. In the downstream section, a jet forms just behind the throat exit surrounded by recirculatory flow, which extends along the full length of the section. Winding of the jet downstream is due to its interaction with the moving smallest vortices. Details of this recirculatory flow are displayed in Fig. 14, which show blowup views of the flow just above the vena contracta at $t = 4.65$ s for the models of Fig. 12. Inspection of these figures shows that the vortices appearing downstream on both sides of the vena contracta

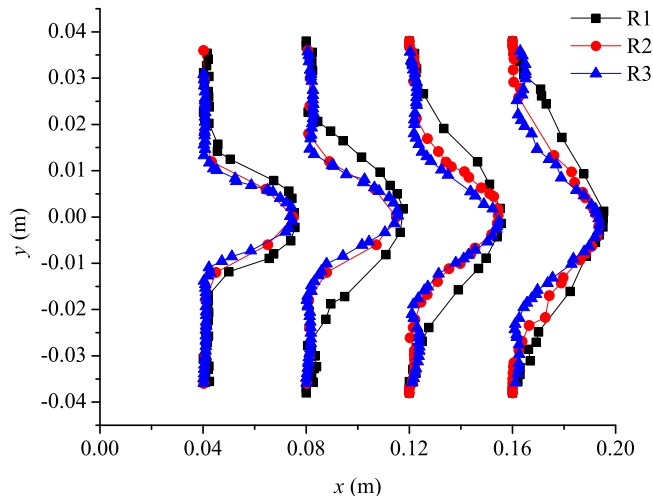


Figure 15: Comparison of the streamwise velocity profiles at successive stations in the downstream section of the constricted channel for models R1, R2, and R3 at $t = 4.65$ s.

are damped in model R1 (top frame) compared to models R2 (middle frame) and R3 (bottom frame), implying that neglecting the anisotropic term in Eq. (29) affects the structure of the flow. Also the reattachment length at $t = 4.65$ and 6.0 s is much shorter in model R1 (≈ 0.10 m) compared to model R3 (≈ 0.24 m). As shown in Figs. 12 and 13, the flow structure for model R2 closely follows that shown for model R3 with a longer downstream channel, demonstrating that the feedback noise from the outlet boundary is also greatly reduced for this test.

Figures 15 and 16 show longitudinal velocity profiles for models R1, R2, and R3 at successive streamwise stations along the downstream section for the same times of Figs. 12 and 13, respectively. In both figures, the squares depict the profiles for model R1, while the dots and triangles correspond to the profiles for models R2 and R3, respectively. It can be clearly seen that there is a very good correspondence between the profiles for models R2 and R3 for all stations at both times. In contrast, the profiles of model R1 substantially deviate from those of models R2 and R3 on both sides of the centreline and towards the channel walls, with the magnitude of the deviations increasing close to the outlet. The good correspondence between the results of models R2 and R3 proves the efficiency of the nonreflecting outlet

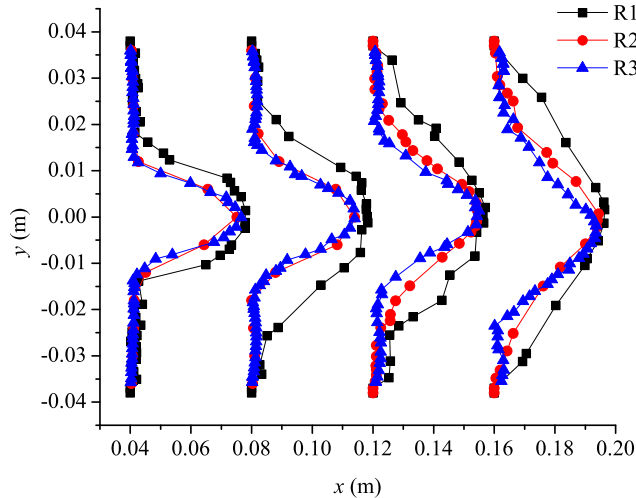


Figure 16: The same as Fig. 15 at $t = 6.0$ s.

boundary conditions when the anisotropic diffusion term is accounted for in Eq. (29), which allows us to work with smaller sizes of the computational domain.

6. Flow in a square-sectioned 90° pipe bend

We now assess the performance of the nonreflecting outlet boundary conditions on a full 3D test problem. We simulate the steady, turbulent flow in a 90° section of a curved square pipe at $Re = 40000$. The numerical results are compared with experimental measurements [36] and numerical simulations carried out with the software package FLUENT 6.2 [37] for the same parameters. The geometrical model and parameters are the same employed by Sudo et al. [36] in their experimental investigation.

The pipe geometry is shown in Fig. 17. The pipe has a square cross-section measuring $l \times l = 80 \text{ mm} \times 80 \text{ mm}$ and a 90° bend of curvature radius $R = 160 \text{ mm}$ connected at its both ends with a horizontal straight duct upstream of $L_h = 2 \text{ m}$ long and a vertical straight duct downstream of length $L_v = 1.6 \text{ m}$. At the inlet, a flat velocity profile with $v_c = 7.4 \text{ m s}^{-1}$ is assumed in correspondence with the experimental bulk mean velocity. With these parameters, the curvature radius ratio is $2R/l = 4$ and the Dean number is

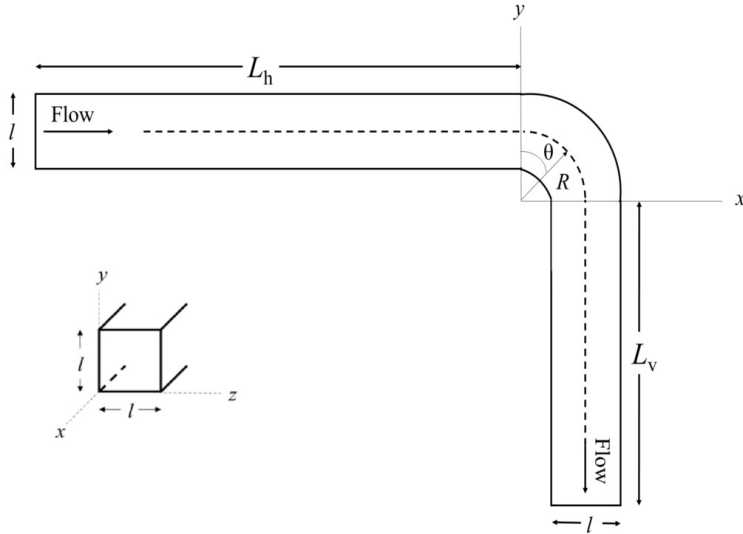


Figure 17: Schematic diagrams of the pipe bend and coordinate system.

$D = \text{Re} \sqrt{l/2R} = 2 \times 10^4$, with $\text{Re} = v_{\text{in}} l / \nu = 4 \times 10^4$, where ν is the kinematic viscosity. To achieve a comparable spatial resolution to the simulations by Rup et al. [37], we fill the pipe volume with 1.03 million particles initially at rest and uniformly spaced in all three coordinate directions ($\Delta x = \Delta y = \Delta z = 3$ mm). The particles are given an initial smoothing length $h \approx 6.06$ mm and Eq. (4) is used as the pressure-density relation with $c_0 = 5$ m s⁻¹.

In order to provide direct comparison with the experimental data of Sudo et al. [36] and the numerical calculations of Rup et al. [37], Fig. 18 depicts profiles of the longitudinal mean velocity in the horizontal plane including the duct axis at three different streamwise stations: (a) in the horizontal duct at 0.08 m from the entrance of the bend (corresponding to $x = 1.92$ m from the inlet, i.e., $z'/d = -1$ in Sudo et al. [36] notation), (b) within the bend at $\theta = 60^\circ$, and (c) down the vertical duct at $y = 0.8$ m from the bend exit (i.e., $z'/d = 10$ in Sudo et al. notation). We may see that the SPH profiles (solid lines) are in reasonably good agreement with the experimental data (dots) and the FLUENT simulations (dashed lines). Because of the assumption of a flat velocity profile at the inlet, the flow in the SPH and FLUENT simulations is not fully developed at $x = 1.92$ m from the inlet (top frame) and therefore the velocities around the pipe centreline are underestimated compared to the experimental data. As the flow enters the bend, the

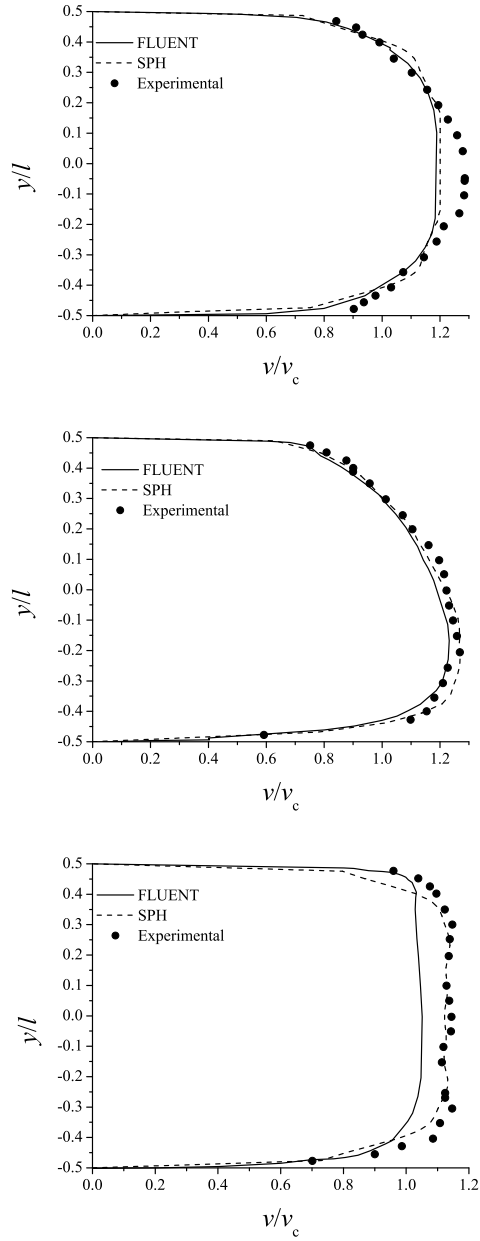


Figure 18: Profiles of longitudinal mean velocity at different streamwise stations: at $x = 1.92$ m from the inlet (top frame), within the bend at $\theta = 60^\circ$ (middle frame), and down the vertical duct at $y = 0.8$ m from the bend exit (bottom frame). The SPH results (dashed lines) are compared with the experimental measurements of Sudo et al. [36] (dots) and the FLUENT calculations of Rup et al. [37] (solid lines). The pipe cross-section and longitudinal velocity are normalized to the hydraulic diameter $l = 80$ mm and the inlet velocity $v_c = 7.4 \text{ m s}^{-1}$, respectively.

longitudinal velocity profile distorts as a secondary flow grows. At $\theta = 60^\circ$ within the bend (middle frame), the fluid flow is faster towards the inner wall due to the larger pressure gradients there. The SPH calculation reproduces reasonably well the asymmetric profile and closely matches the experimental and FLUENT profiles at this station. Away from the bend exit at $y = 0.8$ m (bottom frame), the secondary flow attenuates and the vortex breaks down. At this station, the SPH simulation reproduces very well the experimental flow velocity front, meaning that the nonreflecting outlet boundary conditions are not influencing the flow in the elbow and along the vertical duct. In contrast, the FLUENT calculation underestimates the front velocity by about 10%. Given the good matching of the FLUENT results with the experimental measurements at $\theta = 60^\circ$, the 10% deviation in the front velocity at $y = 0.8$ m from the bend exit may be caused by some influence from the outlet boundary condition.

7. Conclusions

In this paper, we have described a procedure, based on Jin and Braza's [18] method, for modelling nonreflecting outlet boundary conditions for incompressible Navier-Stokes flows using the method of smoothed particle hydrodynamics (SPH). The method, which was originally developed for two-dimensional (2D) flows, was also generalized to three-space dimensions (3D). As it is common practice in SPH, the method involves inflow and outflow zones of particles, which are external to the fluid domain. A reservoir zone is designed to temporarily store particles, which is useful in most applications where the rate of outflowing and inflowing particles is not the same. Non-reflecting outlet boundary conditions are implemented here by allowing the particles that leave the computational domain and enter the outflow zone to move according to an outgoing wave equation for the velocity field so that feedback noises from the boundary are effectively reduced. For unsteady, unidirectional flows, the method reduces to the well-known Orlanski wave equation, while for steady-state flows it takes the form of a zero diffusive boundary condition.

The performance and accuracy of the method was assessed against several 2D tests, including the unsteady, plane Poiseuille flow, flow between inclined plates, the Kelvin-Helmholtz instability in a channel, and flow in a constricted channel. The performance of the method was also assessed for a 3D test problem involving the turbulent flow in a square-sectioned 90°

pipe bend. For this test, the numerical SPH results were compared with experimental measurements and previous numerical analysis obtained using the software package FLUENT 6.2. In general, the results show that spurious waves incident on the outlet are effectively absorbed, inhibiting feedback noises and allowing us to reduce the length of the computational domain. In addition, steady-state laminar flows can be maintained stably for much longer times compared to periodic boundary conditions. The method is stable and has the advantage of being easily implemented for other types of incompressible flows at low and moderate Reynolds numbers, as may be the case of flows around obstacles and free shear layer flows with transition towards turbulence, among others.

Acknowledgement

We thank the reviewers who have provided a number of comments and suggestions that have greatly improved the style and content of the paper. The calculations of this paper were performed using the computing facilities of ABACUS-Cinvestav. This work was partially supported by ABACUS under CONACyT grant EDOMEX-2011-C01-165873 and by the Departamento de Ciencias Básicas of the Universidad Autónoma Metropolitana-Azcapotzalco (UAM-A) through internal funds.

References

References

- [1] R. L. Sani, P. M. Gresho, Résumé and remarks on the open boundary condition minisymposium, *Int. J. Numer. Meth. Fluids* 18 (10) (1994) 983–1008.
- [2] M. Lastiwka, M. Basa, N. J. Quinlan, Permeable and non-reflecting boundary conditions in sph, *Int. J. Numer. Meth. Fluids* 61 (7) (2009) 709–724.
- [3] S. Dong, G. E. Karniadakis, A. Ekmekci, D. Rockwell, A combined direct numerical simulation - particle image velocimetry study of the turbulent near wake, *J. Fluid Mech.* 569 (2006) 185–207.

- [4] S. Dong, G. E. Karniadakis, C. Chrysostomidis, A robust and accurate outflow boundary condition for incompressible flow simulations on severely-truncated unbounded domains, *J. Comput. Phys.* 261 (2014) 83–105.
- [5] J. P. Morris, P. J. Fox, Y. Zhu, Modeling low reynolds number incompressible flows using sph, *J. Comput. Phys.* 136 (1997) 214–226.
- [6] E.-S. Lee, C. Moulinec, R. Xu, D. Violeau, D. Laurence, P. Stansby, Comparisons of weakly compressible and truly incompressible algorithms for the sph mesh free particle method, *J. Comput. Phys.* 227 (2008) 8417–8436.
- [7] M. S. Shadloo, A. Zainali, S. H. Sadek, M. Yildiz, Improved incompressible smoothed particle hydrodynamics method for simulating flow around bluff bodies, *Comput. Meth. Appl. Mech. Eng.* 200 (2011) 1008–1020.
- [8] A. Vazquez-Quesada, M. Ellero, Sph simulations of a viscoelastic flow around a periodic array of cylinders confined in a channel, *J. Non-Newton. Fluid Mech.* 167-168 (2012) 1–8.
- [9] S. Khorasanizade, J. F. Pinto, J. M. M. Sousa, On the use of inflow/outflow boundary conditions in incompressible, internal flow problems using smoothed particle hydrodynamics, 6th European Congress on Computational Methods in Applied Sciences and Engineering (EC-COMAS 2012), Vienna University of Technology, 2012, pp. 7050–7059.
- [10] A. J. Chorin, Numerical solution of the navier-stokes equations, *Math. Comput.* 22 (1968) 745–762.
- [11] R. Témam, Sur l’approximation de la solution des équations de navier-stokes par la méthode des pas fractionnaires (ii), *Arch. Ration. Mech. Anal.* 33 (5) (1969) 377–385.
- [12] S. J. Cummins, M. Rudman, An sph projection method, *J. Comput. Phys.* 152 (1999) 584–607.
- [13] L. J. P. Timmermans, P. D. Mineev, F. N. van de Vosse, An approximate projection scheme for incompressible flow using spectral elements, *Int. J. Numer. Meth. Fluids* 22 (1996) 673–688.

- [14] S. M. Hosseini, J. J. Feng, Pressure boundary conditions for computing incompressible flows with sph, *J. Comput. Phys.* 230 (2011) 7473–7487.
- [15] S. Khorasanizade, J. M. M. Sousa, J. F. Pinto, On the use of a time-dependent driving force in SPH simulations, *Spheric*, Prato, Italy, 2012, pp. 92–98.
- [16] M. Becker, M. Teschner, Weakly compressible sph for free surface flows, *SCA '07 Proceedings of the 2007 ACM SIGGRAPH/Eurographics Symposium on Computer Animation*, ACM Press, 2007, pp. 209–217.
- [17] C. Liang, J. Huang, W. Shi, A new treatment for boundary laminar flow inlet or outlet in sph, *J. Software Eng.* 8 (4) (2014) 321–327.
- [18] G. Jin, M. Braza, A nonreflecting outlet boundary condition for incompressible unsteady navier-stokes calculations, *J. Comput. Phys.* 107 (1993) 239–253.
- [19] R. A. Dalrymple, B. D. Rogers, Numerical modeling of water waves with the sph method, *Coastal Eng.* 53 (2006) 141–147.
- [20] A. Yoshizawa, Statistical theory for compressible turbulent shear flows, with application to subgrid modeling, *Phys. Fluids A* 29 (1986) 2152–2164.
- [21] J. J. Monaghan, Smoothed particle hydrodynamics, *Annu. Rev. Astron. Astrophys.* 30 (1992) 543–574.
- [22] L. D. Libersky, A. G. Petschek, T. C. Carney, J. R. Hipp, F. A. Alahdadi, High strain lagrangian hydrodynamics, *J. Comput. Phys.* 109 (1993) 67–75.
- [23] A. Colagrossi, M. Landrini, Numerical simulation of interfacial flows by smoothed particle hydrodynamics, *J. Comput. Phys.* 191 (2003) 448–475.
- [24] E. Lo, S. Shao, Simulation of near-shore solitary wave mechanics by an incompressible sph method, *Appl. Ocean Res.* 24 (2002) 275–286.
- [25] L. Hernquist, N. Katz, *Treesph: A unification of sph with the hierarchical tree method*, *Astrophys. J. Suppl. Series* 70 (1989) 419–446.

- [26] R. Vacondio, B. D. Rogers, P. K. Stansby, P. Mignosa, J. Feldman, Variable resolution for sph: A dynamic particle coalescing and splitting scheme, *Comput. Methods Appl. Mech. Engrg.* 256 (2013) 132–148.
- [27] W. Dehnen, H. Aly, Improving convergence in smoothed particle hydrodynamics simulations without pairing instability, *Mon. Not. R. Astron. Soc.* 425 (2) (2012) 1068–1082.
- [28] P. M. Gresho, Some current cfd issues relevant to the incompressible navier-stokes equations, *Comput. Methods Appl. Mech. Engrg.* 87 (1991) 201–252.
- [29] R. Glowinski, Finite element methods for navier-stokes equations, *Annu. Rev. Fluid Mech.* 24 (1992) 167–204.
- [30] M. Braack, P. B. Mucha, Directional do-nothing conditions for the navier-stokes equations, *J. Comput. Math.* 32 (5) (2014) 507–521.
- [31] A. Sohankar, C. Norberg, L. Davidson, Low-reynolds number flow around a square cylinder at incidence: study of blockage, onset of vortex shedding and outlet boundary condition, *Int. J. Numer. Meth. Fluids* 61 (1998) 39–56.
- [32] J. Z. Lin, X. D. Ruan, B. G. Chen, *Fluid Mechanics*, Tsinghua University Press, Beijing, 2005.
- [33] C. X. Liang, C. Y. Zhang, H. Y. Liu, Z. R. Qin, Q. Wang, Modeling low reynolds number incompressible flows with curved boundaries using sph, *Int. J. Numer. Meth. Fluids* 68 (2012) 1173–1188.
- [34] S. Chandrasekhar, *Hydrodynamic and Hydromagnetic Stability*, Dover Publications, New York, 1981.
- [35] D. J. Price, Modelling discontinuities and kelvin-helmholtz instabilities in sph, *J. Comput. Phys.* 227 (2008) 10040–10057.
- [36] K. Sudo, M. Sumida, H. Hibara, Experimental investigation on turbulent flow in a square-sectioned 90-degree bend, *Exp. Fluids* 30 (2001) 246–252.
- [37] K. Rup, L. Malinowski, P. Sarna, Measurement of flow rate in square-sectioned duct bend, *J. Theoret. Appl. Mech.* 49 (2) (2011) 301–311.